Journal of Wind Engineering & Industrial Aerodynamics 188 (2019) 194–206

Contents lists available at ScienceDirect

Journal of Wind Engineering & Industrial Aerodynamics

journal homepage: www.elsevier.com/locate/jweia

Flow structure between freight train containers with implications for aerodynamic drag

Siavash Maleki *, David Burton, Mark C. Thompson

Fluids Laboratory for Aeronautical and Industrial Research (FLAIR), Department of Mechanical and Aerospace Engineering, PO Box 31, Monash University, 3800, Australia

ARTICLE INFO

Keywords:
Computational fluid dynamics (CFD)
Hybrid RANS/LES
Freight train
Train aerodynamics
Bluff body flow

ABSTRACT

Predictions from embedded-LES are presented of a model of a section of a double-stacked freight wagon subjected to different local loading configurations. In total, 15 different upstream (G_{front}) and downstream (G_{base}) gap spacings were simulated to characterise the change in the flow topology.

The mean flow fields indicate that the inter-wagon flow undergoes a significant topology change over the range of $G_{front} = 1.77W$–$3.23W$ (W = wagon width). For $G_{front} \leq 1.77W$, the mean recirculating flow in the gap covers its entire length. In contrast, for $G_{front} \gtrsim 3.23W$, the complete wake closure for the upstream wagon occurs enabling the upstream shear layers to impinge on the entire downstream surface, in turn, increasing the rate of change of drag force as G_{front} is increased. The change in the wake shedding frequency, directly affecting the base pressure and consequently the drag, due to the variation in G_{front} and G_{base}, is presented.

1. Introduction

Improving fuel economy and reducing blackhouse emissions of freight trains has been an ongoing challenge, but one that is strongly affected by loading configuration. At least four major reasons may lead to differences in the way a freight train is loaded. Firstly, the dimensions of shipping containers vary in each of length, width and height. Secondly, at intermodal terminals, containers are loaded differently depending on their specific geometry. Thirdly, the typical arrangement of the containers on each train can vary. They can be loaded either single-stacked or double-stacked, as is examined in this study, which doubles the height-to-width ratio. Finally, during the journey, the loading pattern of an entire train could be subjected to significant change through the introduction of new containers or removal of existing ones at terminals along the route. Each of these factors significantly affects the loading pattern of a freight train, leading to different aerodynamic performance.

Another difficulty in modelling the aerodynamic freight train is their extreme length which could reach up to ~2 km. The length-to-height ratio of freight trains ($L/H = 250-500$) is greater than that of the high-speed passenger trains ($L/H = 25-200$) (Bell et al., 2016), (Baker et al., 2014). At this stage, neither full-scale experimental nor full-resolved numerical investigations of complex bluff bodies with such extreme lengths are possible.

Many researchers have evaluated the effects of wagon position within a train together with the local inter-wagon spacing on aerodynamic drag. Gielow and Furlong (1988) performed extensive wind-tunnel tests to develop an aerodynamic drag database for train resistance simulations. In one of their tests, the position of a full-scale wagon, instrumented for force measurements, was incrementally varied from the 2nd to the 30th position, to study the influence of the position of a wagon within a train. Their measurements show a rapid decay in drag as the test car was moved downstream to the 8th position, after which it reached a constant value.

Watkins et al. (1992) conducted wind-tunnel tests in an attempt to evaluate the minimal configuration for modelling an individual wagon positioned in the middle section of a train. No significant change in drag was found for the middle wagon, when at least 1.5 wagons were placed upstream and 0.5 wagons downstream. Golovanevskiy et al. (2012) employed the Reynolds-Averaged Navier-Stokes (RANS) approach to model open cargo trains consisting of a locomotive, and 10, 12 and 14 wagons. Their findings showed that the locomotive and the last wagon only affected the aerodynamic drag of the first and last three wagons. All other wagons in a long train experienced a similar drag coefficient.

To assess the effect of different loading configurations of freight trains, Li et al. (2017) took an approach where they considered the loaded train to be the summation of localised effects of individual wagons. Their setup consisted of seven wagons in tandem: three initial

* Corresponding author.
E-mail address: siavash.maleki@monash.edu (S. Maleki).

https://doi.org/10.1016/j.jweia.2019.02.007
Received 24 October 2018; Received in revised form 17 February 2019; Accepted 18 February 2019
Available online 11 March 2019

wagons followed by a test wagon and then three trailing wagons. To determine the localised influence of loading patterns, the test wagon was pressure tapped, to enable the forward and backward-facing surface pressure distributions to be determined. In wind-tunnel tests, upstream and downstream gaps (G_{front},G_{base}) at the front and rear of the test wagon were varied incrementally over 7 gap sizes, resulting in a combination of 49 upstream and downstream gap spacings. This approach enabled an estimate of the pressure drag to be determined from these upstream and downstream pressure measurements.

The influence of gap spacing between wagons on aerodynamic drag has been extensively researched. The full-scale tests conducted by Paul et al. (2009) showed 30% drag reduction as the inter-wagon gap was reduced from 1.6m to 0.5m. Watkins and Saunders (1992) conducted wind-tunnel testing to obtain the drag profile associated with inter-wagon gaps and cross-wind angle. They showed an increase in inter-wagon gap size increased drag at each angle of cross-wind. They also reported that the trend of drag growth with respect to cross-wind angle was parabolic.

Attempt was made to model the flow conditions for a wagon in an infinitely long train. Östh and Krajnović (2012) performed a LES simulation in which a half of wagon was modelled upstream and downstream of the wagon. Periodic streamwise boundary conditions were used to map the outlet condition to the inlet. The drag reported for this simulation was approximately 10% of that for a wagon in freestream. However, applying the periodic streamwise boundary condition leads to constant development of the boundary layer along the length of a train, meaning the upstream flow condition of the wagon is constantly being changed. Hence, the predicted drag coefficient does not represent the drag experienced by a wagon in a certain longitudinal position within the train.

Recently, McArthur et al. (2016) has extensively characterised both the steady state and transient near wake structure of the *Ground Transportation System* (GTS) as ground proximity was varied. For the baseline case, the time-averaged flow of the GTS consisted of a vertically asymmetric wake, with a large spanwise vortex close to the lower part of the base for the baseline case. It was shown that reducing the ground proximity resulted in significant changes to wake topology. At the lowest ground clearance tested, the time-average upper vortex was enlarged, while the lower vortex was reduced in size. With an increase of the time-averaged upper vortex, the base pressure is likely to drop, leading to reduction in drag, as its low pressure core moves downstream further away from the base surface. Regardless of the size of the ground clearance, the lower vortex was found to be almost quasi-steady and a considerable source of base suction as it spent the majority of time in close proximity the base of the GTS model. The wake profile of the GTS model at a minimum ground proximity is expected to be the closest to that of the wagon subjected to a large downstream gap size, due to the presence of the downstream wagon tray restricting the flow from underneath the wagon to emerge into the gap.

In addition to the effect of ground clearance, the ground motion significantly influences the drag of ground (heavy) vehicles. The importance of the ground condition on flow structures around vehicles has been investigated by many researchers, such as Krajnovic and Davidson (2005), Fago et al. (1991), Strachan et al. (2007), etc. Krajnovic and Davidson (2005) performed Large Eddy Simulations (LES) on the Ahmed body with a slant angle of 25° with stationary and moving grounds. Their predictions showed that the vehicle experienced 8% less drag with a moving floor than with a stationary ground. Despite the influence of the ground motion on aerodynamic forces, the stationary ground condition was employed for all simulations in this study. This approach was taken to correctly match the flow condition of wind-tunnel experiment conducted by Li et al. (2017), in which the vehicle reference frame was adopted.

The authors (Maleki et al., 2017) have previously compared the performance of Embedded Large Eddy Simulation (ELES), Scale-Adaptive Simulation (SAS), Unsteady Reynolds Averaged Navier-Stokes (URANS) and RANS with the wind-tunnel measurements obtained by Li et al. (2017) to accurately predict the flow around a double-stacked wagon freight wagon, in freestream and within a train, but only for a single gap size. The parameters examined by these turbulence modelling approaches were the front and rear surface pressures, aerodynamic drag, skin friction lines and boundary layers on the top surface of a double-stacked freight wagon. The selected loading configuration is $G_{front} = 9.38W$ and $G_{base} = 3.23W$, where the upstream gap size is 1.5 times larger than the largest gap size presented here. The test wagon subjected to this loading configuration behaves much closer to an isolated wagon as opposed to a wagon within a train, subjected to a relatively small or medium gap size, as the flow travels inside a very large upstream gap size, equivalent to 1.5 empty wagon. Overall, it was shown that RANS, URANS and SAS do not provide as close predictions as ELES to wind-tunnel results, particularly for the regions flow separation occurs.

The primary objective of this paper is to improve our understanding of the mean and time-varying flow topology of a double-stacked wagon subjected to varying local loading patterns, in particular, characterising the reversed flow in the separated regions, and specifically the flows inside the different-sized upstream and downstream gaps and the influence of varying both together. In parallel wind-tunnel experiments (Li et al. (2017)), the separated regions and recirculation zones could not be characterised due to the limited acceptance cone of the Cobra probe (±45°) used to measure the velocity field. However, experimental surface pressure and direct drag measurements have revealed that there is a rapid increase in pressure drag as the front gap was increased over the range $1.77W < G_{front} < 3.23W$, which is presumably associated with a change in the flow topology within and around the gap. The key aims of this study are therefore to: (i) model this change to the flow; and (ii) understand the underlying mechanism(s) behind it. This knowledge could assist rolling stock engineers to modify the flow within interwagon gaps to reduce their incremental drag contributions.

2. Model description

The model employed in our numerical simulations is a double-stacked container wagon resembling that tested by Li et al. (2017) in the 450 kW closed-circuit wind tunnel at Monash University. The test section of this wind tunnel is $16 \times 2 \times 2\text{m}^3$ ($L \times W \times H$), which gives a wind-tunnel blockage of 2.4%. The experimental model is a 1/14.6th scale model of 14.6 m double-stacked container wagon, with $L = 1000$mm, $W = 171$mm and $H = 438$mm representing a section of a freight train. The ground clearance was $E = 28$mm, corresponding to a wheel radius at full-scale of a 410 mm wheel. All additional features, such as under body bogies and panel ribbing, were excluded from the experimental model; the wagon was simplified to a rectangular prism. The experimental setup consisted of seven wagons aligned longitudinally, as shown in Fig. 1. All wagons had identical geometry excluding the leading wagon, which has a rounded nose, similar to that of an Ahmed body (Ahmed, 1983), to limit front-edge flow separation.

To simplify the train geometry and to focus on the local loading configuration, the spaces between upstream and downstream wagons were covered, in line with the experimental model. To test the influence of this simplification, the model was tested in the wind-tunnel with the smaller (standard) inter-wagon gaps covered and uncovered. Negligible change in pressure drag coefficient (C_{Dp}) was reported by Li et al. (2017) for the four different gap sizes tested. A full description of the experimental setup can be found in (Li et al., 2017).

In addition to these simplifications, the influences of boundary-layer thickness, moving ground, cross-wind (yaw), the container's arrangement (single-stacked or double-stacked) are also not considered as part of this restricted investigation. The stationary ground was selected to match the flow condition of wind-tunnel experiment. The reason for overlooking the other factors was to reduce the parameters considered herein and to focus on the effect of the upstream and downstream gap size combinations.

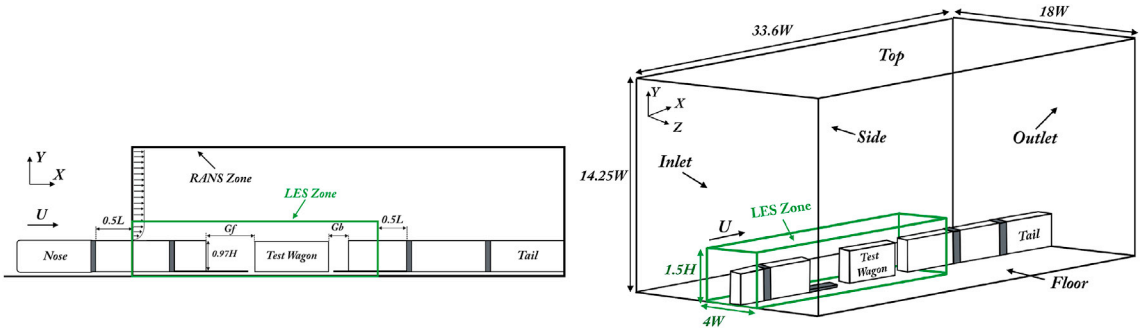

Fig. 1. Placement and dimensions of multi double-stacked wagons within the computational domain, showing a front and base gaps with the LES zone marked.

3. Computational domain and boundary conditions

In the present work, multiple wagons consisting three wagons upstream and downstream of the test wagon are positioned with varying upstream (G_{front}) and downstream gap (G_{base}) sizes. As shown in Table 1, in total 15 different configurations were simulated. Both G_{front} and G_{base} were incrementally varied through 7 sizes covering the range $0.3W \leq G_{front,base} \leq 6.46W$, while the opposite gap was kept constant at $0.3W$, resulting in 13 different loading configurations. Note that $0.3W$ is the smallest gap size between two containers, while $6.46W$, the largest gap size studied here, is equivalent to one empty container wagon. Also, two additional front gap sizes, $G_{front} = 3.23W$ and $G_{front} = 5.06W$ at $G_{base} = 5.06W$ were simulated to study the effects of an increase in G_{front} on the wake topology and base pressure of the test wagon.

The inlet of the computational domain was placed at the middle of the second wagon, as shown in Fig. 1, to reduce the overall computational cost, relative to that required to reproduce the wind-tunnel setup. To enable this, the experimental boundary layer profile was measured at the middle of the second wagon and on the splitter plate for the gap combination of $G_{front} = 0.3W$ and $G_{base} = 0.3W$ using a Cobra probe,[1] and was reproduced as the inlet condition for all simulations. The simulated boundary layer profile at the inlet had a $30\,ms^{-1}$ freestream velocity corresponding to a Reynolds number based on wagon width of $Re_w = 0.3 \times 10^6$, matching the wind-tunnel experiment.

All simulations in this study were undertaken using the ELES approach. This is a zonal hybrid RANS/LES methodology designed to capture the instantaneous flow in the region of focus of a computational domain, reducing the computational cost significantly. In the ELES approach, the domain is split into RANS and LES regions in the pre-processing stage to predefine the RANS and LES zones. The conversion from modelled turbulence (RANS) to resolved turbulence (LES) is carried out at the RANS/LES interface (Mathey et al., 2006).

The different domains of the zonal hybrid RANS/LES approach are illustrated in Fig. 1. In this study, the inlet of the LES zone corresponded to the inlet of the computational domain. As a result of defining the LES zone from the inlet, the predictions obtained from these ELES simulation are effectively the same as those of an LES simulation, with the encasing RANS zone reducing blockage and extending the outflow region. Post priori, it is clear that the generated vortical structures are retained within the LES zone. Furthermore, the outlet of LES zone, where the resolved turbulent structures entered into the RANS zone, is located sufficiently far downstream of the base gap to cause negligible effects on the flow in the region of interest.

To generate a time-varying inlet condition at the LES inlet zone, a random 2*D* Vortex Method (VM) was employed, as it is the most widely used method in ANSYS Fluent. This approach added perturbations on the time-averaged experimental velocity profile reproduced at the inlet using a fluctuating two-dimensional vorticity field. The VM method is based on the Lagrangian form of the 2D evolution equation of the vorticity and the Biot-Savart law (Mathey et al., 2006). To solve this equation, a particle discretisation is used. The vortex points randomly travel downstream and carry information about the vorticity field. ANSYS Fluent uses a simplified linear kinematic model (LKM) for the streamwise velocity fluctuations, which is derived from a linear model, mimicking the influence of the two-dimensional vortex in the streamwise mean velocity field. The two scales of k and ω are the input parameters used to the VM. Post-priori, it is clear that the VM provides sufficiently realistic turbulent

Table 1
ELES predictions of pressure drag coefficient for the various (G_{front}, G_{base}) combinations, as a function of mesh and time resolution. Experimental drag coefficients from Li et al. (2017) are shown for comparison.

Gap Combination	Mesh	Cells	$\Delta t/T_{ref}$	C_{Dp} (ELES)	C_{Dp} (Exp)
$G_{front} = 0.3W$ and $G_{base} = 0.3W$	*Fine*	15.5 million	0.006	0.02	0.04
$G_{front} = 1.04W$ and $G_{base} = 0.3W$	*Fine*	15.75 million	0.006	0.08	0.1
$G_{front} = 1.77W$ and $G_{base} = 0.3W$	*Fine*	16 million	0.006	0.14	0.16
$G_{front} = 2.5W$ and $G_{base} = 0.3W$	*Fine*	16.2 million	0.006	0.24	0.24
$G_{front} = 3.23W$ and $G_{base} = 0.3W$	*Fine*	16.4 million	0.006	0.38	0.37
$G_{front} = 5.06W$ and $G_{base} = 0.3W$	*Fine*	16.9 million	0.006	0.54	0.53
$G_{front} = 6.46W$ and $G_{base} = 0.3W$	*Fine*	17.2 million	0.006	0.55	0.56
$G_{front} = 0.3W$ and $G_{base} = 1.04W$	*Fine*	16.2 million	0.006	0	0.04
$G_{front} = 0.3W$ and $G_{base} = 1.77W$	*Fine*	16.5 million	0.006	0	0.04
$G_{front} = 0.3W$ and $G_{base} = 2.5W$	*Fine*	17 million	0.006	0	–
$G_{front} = 0.3W$ and $G_{base} = 3.23W$	*Fine*	17.2 million	0.006	0.06	0.09
$G_{front} = 0.3W$ and $G_{base} = 5.06W$	*Fine*	17.5 million	0.006	0.13	–
$G_{front} = 0.3W$ and $G_{base} = 6.46W$	*Fine*	18 million	0.006	0.15	0.16
$G_{front} = 3.23W$ and $G_{base} = 5.06W$	*Fine*	18.4 million	0.006	0.53	–
$G_{front} = 5.06W$ and $G_{base} = 5.06W$	*Fine*	19 million	0.006	0.66	–
$G_{front} = 1.77W$ and $G_{base} = 0.3W$	*Coarse*	4.25 million	0.015	0.1	0.16
$G_{front} = 3.23W$ and $G_{base} = 0.3W$	*Coarse*	4.6 million	0.015	0.34	0.37
$G_{front} = 0.3W$ and $G_{base} = 1.77W$	*Coarse*	4.8 million	0.015	0	0.04
$G_{front} = 0.3W$ and $G_{base} = 3.23W$	*Coarse*	5 million	0.015	0.05	0.09

[1] This device could measure three velocity components in a flow with an acceptance cone angle of 45° and velocity up to 50 m/s, and has a frequency response up to 2000 Hz.

structures at the inlet.

A turbulence intensity of 1% and the ground clearance of the numerical domain was selected in line with the wind-tunnel experiment. A no-slip boundary condition was employed at the bottom of the domain. A zero-shear wall condition was used at both the top and side of the computational domain. The outlet of the computational domain is set as a zero pressure outlet located three wagons downstream of the test wagon, which is assumed to be sufficient to induce the minimal upstream effects on the flow in the regions of interest.

4. Numerical method

The commercial flow-simulation package ANSYS FLUENT version 16.1 was used for the simulations. The RANS turbulence model used in non-LES zones for this study was the *SST* $k-\omega$ model. The SIMPLEC algorithm with the *Bounded Central Difference* scheme were utilised for time integration and spatial discretisation, respectively. Within the LES zones, the Wall-Modelled Large-Eddy Simulation (WMLES) turbulence model was selected due to otherwise high cost of resolving the near-wall region using standard LES at the Reynolds number studied. The WMLES approach significantly lowers the mesh resolution requirements of LES at the wall. It models the flow close to the wall based on a RANS mixing length model, and resolves the flow further away with LES, allowing for a coarser near wall grid resolution than required by LES. This assumes that the fine-scale near-wall dynamic turbulent structures do not have a significant effect on the separated regions and wake.

The time-averaged pressure distribution calculated in this study is expressed in terms of the local pressure coefficient. This is defined as

$$C_p = \frac{P_t - P_{\text{ref}}}{0.5\rho U_\infty^2}. \tag{1}$$

Here, P_t is the time-averaged static pressure, U_∞ is the uniform wind speed, ρ is the density and P_{ref} is a suitable reference pressure taken at a centreline point on top surface of the wagon at $x = 0.75L$. It was chosen far downstream to allow the boundary layer to recover from the upstream separation/recirculation regardless of front gap size. Both numerical and experimental C_p calculations used this point as a reference pressure due to the fact that pressure gradient in the numerical simulation is usually negligible, while it tends to be non-negligible in wind-tunnel flows. Hence, choosing P_{ref} over a standard upstream wind-tunnel static-pressure reading minimises the influence of the wind-tunnel pressure gradient, which adversely affects the comparison between the numerical and experimental data.

In order to calculate the pressure drag coefficient (C_P), the pressure is integrated over the front and base surface to give an area-averaged pressure coefficient (C_P). The difference between the front surface pressure coefficient (C_{Pfront}) and base surface pressure coefficient (C_{Pbase}) gives the pressure drag coefficient of the wagon C_{Dp},

$$C_{Dp} = C_{P\text{front}} - C_{P\text{base}}. \tag{2}$$

5. Grid and timestep resolution

In this research, ANSYS ICEM-CFD was utilised to generate meshes with various grid resolutions for all simulations. The non-conformal method with hexahedral cells was employed to construct the ELES (zonal) grids, as illustrated in Fig. 2. Due to the large number of simulations conducted together with the availability of detailed experimental data for only a limited set of gap combinations, spatial and temporal resolution studies focused on four gap combinations: $G_{front} = 1.77W$ and $G_{base} = 0.3W$; $G_{front} = 3.23W$ and $G_{base} = 0.3W$; $G_{front} = 0.3W$ and $G_{base} = 1.77W$; and $G_{front} = 0.3W$ and $G_{base} = 3.23W$. For each of these cases, results are reported for two grids, corresponding to *coarse* and *fine* grids and different timesteps. A smaller timestep was selected with the finer grids to ensure the Courant number remained below unity over (almost) the entire domain. This present study follows on from a more complete study on the influence of spatial and temporal resolution based on three grids, corresponding to the equivalent of the *coarse*, *medium* and *fine* grid cases here, but only for one gap size combination. Those results are reported in Maleki et al. (2017).

As an indication of the spatial resolution near solid surfaces, the y^+variation on the test wagon is reported for the combination $G_{front} = 3.23W$ and $G_{base} = 0.3W$. In this case, y^+varied between 0.5 and 4.8 over the front surface of the test wagon, with an average of 1.3. The y^+on the base surface showed $y^+ \sim 0.25$–5, providing an average value of 0.96. Additionally, y^+on the side surface was ~0.5–5.75, giving an average of 2.5. Finally, over the entire top surface of the wagon y^+varies between 1 and 8, with an average value of 4.2.

While the y^+values used in this study are slightly higher than the recommended value of $y^+ \simeq 1$, it should be noted that WMLES has the ability to tolerate higher y^+values (Menter). To verify whether the grid resolution used in the ELES simulations using WMLES was sufficient to satisfactorily resolve the inner boundary layer, a comparison was made between the predictions of ELES with $y^+ \simeq 1$ and the ELES simulation reported here for $G_{front} = 0.3W$ and $G_{base} = 3.23W$. The change between the predictions of these two ELES grids was found to be within 1%, confirming the grid resolution reported here was sufficient to accurately capture the inner boundary layer. Note also, that the main objective here is to resolve the flows in the gaps between wagons, rather than the fine-scale boundary layer turbulent structures on the wagon side and top surfaces.

The timestep was normalised by T_{ref}, which is equivalent to the time taken for the fluid to advect one wagon length at the freestream velocity. Time-averaged results are gathered by averaging the flow over at least $50T_{\text{ref}}$ (equivalent to ~ 17 times the fluid travel time to pass through the LES zone) after the flow was first checked to be dynamically steady by comparing averages based on smaller averaging times. The two timesteps selected were equivalent to $\Delta t = 0.015T_{\text{ref}}$ and $\Delta t = 0.006T_{\text{ref}}$. The selected timesteps give the Courant numbers below less than unity over 99% of the cells.

In order to study the influence of temporal and spatial resolution, the predictions were compared with wind tunnel results for the following: (i) the pressure drag coefficient, (ii) the surface pressure distributions on the front, top and back surfaces of the test wagon, and (iii) the velocity profiles on top surface and extending into G_{base}. Table 1 presents the effect of grid and timestep resolution on pressure drag coefficient predictions using the wind-tunnel values for comparison. Fig. 3 displays the predictions of the pressure coefficient, C_p, on the centreline of the front, top and base surfaces for the four cases mentioned above together with the wind-tunnel measurements.

While Fig. 3(b) shows an almost negligible difference in C_p between the coarse and fine grid over the top and base surface of the test wagon, a discernible change in C_p is apparent on the front surface for both $G_{front} = 1.77W$ and $G_{front} = 3.23W$ at $G_{base} = 0.3W$. However, only a minor difference in C_p can be seen between the wind-tunnel results and both fine grids on the front surface, suggesting the separated shear layers travelling inside the upstream gaps were accurately captured with the fine mesh and the smaller timestep.

As is shown in Fig. 3(c), for varying G_{base} at a constant $G_{front} = 0.3W$, almost no change in C_p can be observed over the front face and on the entire top surface of the wagon, except very close to the trailing edge. This suggests further grid refinement and a smaller timestep are unlikely to provide a significantly better prediction over these regions as the flow remains attached to the body of wagon at $G_{front} = 0.3W$. The difference between the coarse and fine meshes pressure fields is minor over the base surface. This once again suggests that little change would result from the use of a finer grid and smaller timestep. Note that despite the slight observable differences between the fine mesh and wind-tunnel results from the middle to the bottom edge of the base surface, the magnitude of pressure is very small.

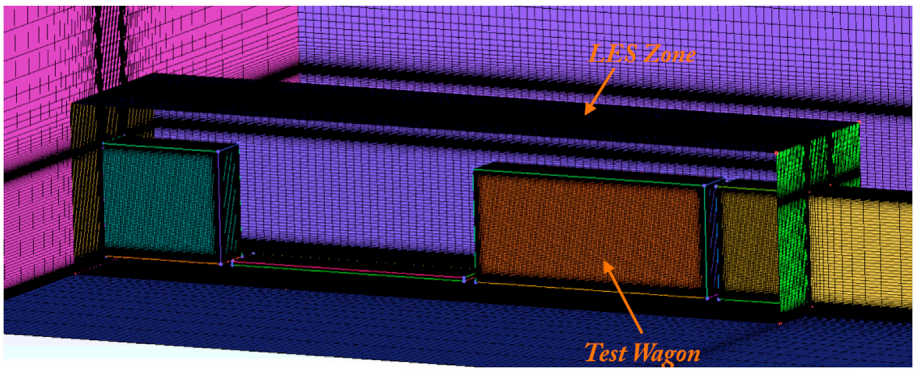

Fig. 2. Section of the non-conformal zonal fine mesh for gap ratio combination $G_{front} = 6.46W$ and $G_{base} = 0.3W$. The high-resolution LES zone is marked, together with the lower resolution surrounding RANS zone. The position of the test wagon is indicated for this gap combination.

Finally, Fig. 4 displays the streamwise velocity for the two ELES cases at the top surface from $x/L = 0.8$ and $x/L = 1$, and extending into the base gap for $G_{front} = 0.3W$ and $G_{base} = 3.23W$, against wind-tunnel results. Note that the experimental velocity profiles were available only for this gap combination. Those wind-tunnel velocity measurements were carried out using a Cobra probe. This device is not able to accurately map the velocity in regions of high turbulence and reversed flow. Hence, only data where less than 20% of velocity vectors lies outside its 45-degree acceptance cone are plotted here. In line with the pressure coefficient discussed above, similar predictions of the streamwise velocity can be seen on the top surface for both ELES cases. The maximum difference between the ELES fine predictions and wind-tunnel measurements is within 5%inside the boundary layer at $x/L = 1$. Considering the lack of reliable experimental data available inside the $G_{base} = 3.23W$ gap, it is very difficult to estimate the over-prediction of the wake length. However, the maximum difference between the experimental data for its lowest reliable point at $x/L = 1.3$ and $x/L = 1.4$ and the ELES fine prediction at the corresponding point is within 16% and 22%, respectively. Once again, due to only a slight change between results from the coarse and fine grids, it seems unlikely that further grid refinement and a smaller timestep would provide a much closer prediction to the experimental data. Overall, the comparisons made between ELES predictions

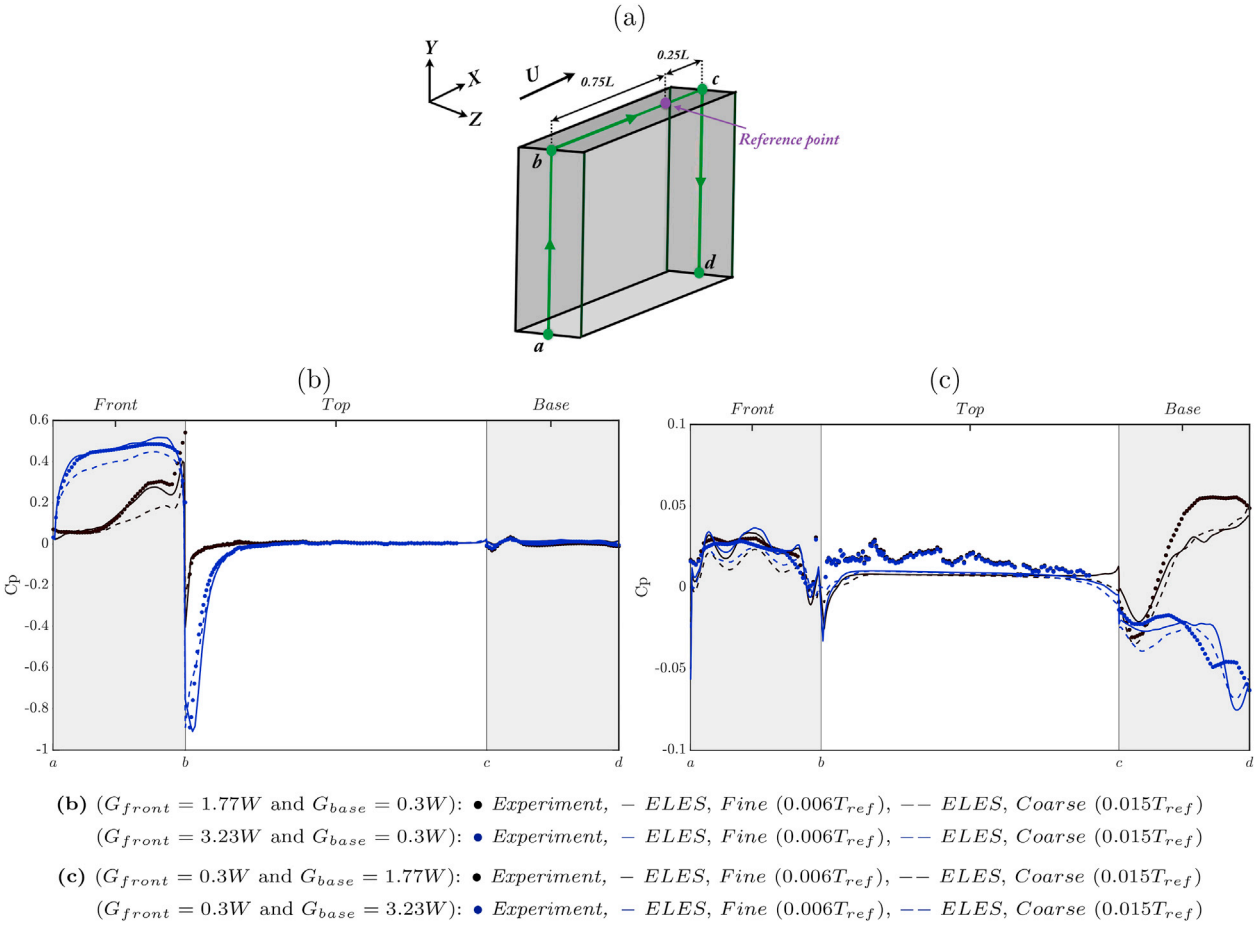

Fig. 3. (a) Coordinate system and the pressure reference point used in the present study. (b) Time-averaged surface pressure coefficient, C_p, of the multiple wagon setup at $G_{front} = 1.77W$ and $G_{base} = 0.3W$ and $G_{front} = 3.23W$ and $G_{base} = 0.3W$ along the centreline ($z = 0$). (c) Time-averaged surface pressure coefficient, C_p, of the multiple wagon setup at $G_{front} = 0.3W$ and $G_{base} = 1.77W$ and $G_{front} = 0.3W$ and $G_{base} = 3.23W$ along the centreline ($z = 0$).

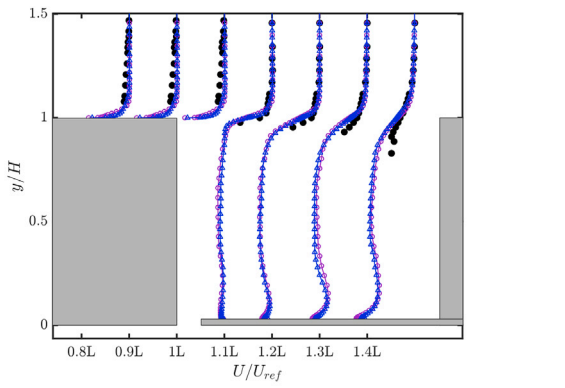

Fig. 4. Time-averaged streamwise velocity profiles in the $x-y$ plane at $z=0$ at the top of the test wagon and extending into the base gap for $G_{front}=0.3W$ and $G_{base}=3.23W$.

and wind-tunnel data on the pressure drag coefficient, surface pressures and velocity profiles suggest that ELES should be able to accurately predict the flow topology of matching wind-tunnel experiments.

6. Results

6.1. Time-averaged analysis

6.1.1. Time-averaged analysis of front and base surface pressures

The predictions of the pressure drag coefficient (C_{DP}) for the various G_{front} and G_{base} combinations against experimental data are presented in Table 1 and Fig. 5. It is clear in Fig. 5 that the front gap size has the dominant effect on controlling the drag. In particular, the rate of change of the drag coefficient with G_{front} is greater than the rate with G_{base}, consistent with the experimental data. The highest rate of change of the drag coefficient occurs over the front gap range $1.77W$–$3.23W$. This has been well predicted by ELES. This change in drag corresponds to a flow topology change inside G_{front}, suggesting that understanding and controlling the flow changes over this range may lead to ways to reduce overall drag.

The drag predictions at $G_{front}=5.06$ and $6.46W$ suggest that further enlargement of G_{front} causes little discernible change in flow topology inside G_{front} as the drag coefficient only increases marginally over this range. Both wind-tunnel and simulation results Maleki et al., (2017) showed $C_{Dp}\simeq 0.93$ for a double-stacked isolated wagon in freestream,

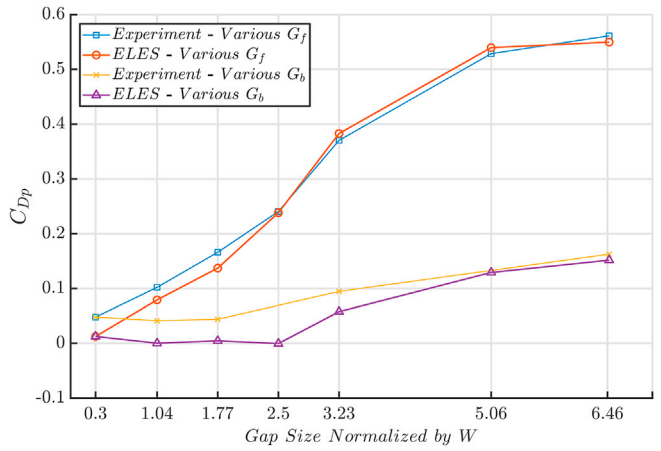

Fig. 5. ELES predictions of pressure drag coefficient for the various G_{front} and G_{base} combinations. Drag coefficients obtained from the experiments of Li et al. (2017) are shown for comparison.

with C_p on the front surface of 0.72. Li et al. (2017) also reported $C_p=0.6$ on the front surface for the two largest gap sizes tested at $G_{front}=9.38W$ and $G_{front}=12.61W$ at $G_{base}=0.3W$. This suggests that the drag experienced by a wagon in the middle section of a train remains almost constant when it is subjected to a gap sizes of $\simeq 6.46W$ or greater. This also indicates that the magnitude of C_p on the front surface of a wagon within a train does not reach to that of a single wagon in freestream. This is primarily due to the shielding effect of the upstream wagon, which lowers the momentum in freestream flow being entrained into the gap, thus weakening the impingement on the front surface of downstream wagon.

The relative contributions of the front and base surface pressure predicted by ELES match the findings of the wind-tunnel tests. ELES accurately predicts that an increase in G_{base} causes little change to the front surface pressure distribution, suggesting that the downstream gap flow has little upstream effect, consistent with the relatively large length-to-height ($L/H=2.28$) ratio of the double-stacked wagon.

Figs. 6 and 7 show coloured pressure contour plots on the front surface for varying G_{front} at constant $G_{base}=0.3W$, and the base surface pressure for varying G_{base} at constant $G_{front}=0.3W$, respectively. The magnitude of pressure on the base surface predicted by ELES however, is slightly different from the experimental results. Specifically, ELES over-predicted the pressure coefficient by $\simeq 0.04$ at the edges and the lower part of the base surface at $G_{base}=0.3W$ and $G_{base}=1.04W$, respectively. The maximum difference in C_p between the ELES and experimental results on the base surface at $G_{base}=1.77W$ and $G_{base}=3.23W$ is around 0.03 (see Fig. 3c), while ELES under-prediction is within $\simeq 0.06$ on the bottom part at $G_{base}=6.46W$. Despite these slight differences, the predicted base pressure distribution reasonably agrees with the wind-tunnel results. The ELES predictions of time-averaged streamlines in the $y=0.5H$ and $z=0$ planes for various G_{front} at constant G_{base} are presented in Figs. 8 and 9, respectively. The purple dashed lines in these figures depict the position of reattachment lines predicted by ELES along the middle of the top/side surface. The time-averaged streamlines provide a qualitative description of the flow structure surrounding the test wagon presenting the relative size of the upstream wagon wake, which strongly affects the magnitude of the front surface pressure as G_{front} is varied.

As speculated by Li et al. (2017), for $G_{front}\leq 1.04W$, the flow field inside the front gap consists of two main counter-rotating vortices shielding the gap from the separated upstream shear layers and allowing them to transfer across the gap. Hence, flow remains fully attached on the top and side surfaces over this gap range.

Figs. 8 and 9 shows a slight separation at the leading edge for $G_{front}=1.77W$ caused by the impingement of shear layers on the upper region of the front surface. This is consistent with the higher pressure in the corresponding regions, as displayed in Fig. 6. The cores of the two symmetrical vortices remain close to the leading edge of the test wagon. Despite the contraction of the lower spanwise vortex, the low pressure region below the middle of vertical line undergoes no significant change, as shown in Fig. 6.

The wake topology undergoes a significant change for $G_{front}=2.5W$. The length of the gap is yet to be large enough for the complete closure of the mean wake to occur. The time-averaged spanwise vortex located at the top is enlarged, which significantly lowers the shear layer impingement point on the upper region of the front surface compared to the $G_{front}=1.77W$ case, causing a uniform pressure distribution over the entire upper region. The spanwise vortex located close to the lower part of the upstream wagon base is significantly contracted, leaving space for the side shear layers to impinge on the lower side regions of the downstream wagon front face, consistent with the higher pressure in the corresponding regions, as shown in Fig. 6. Interestingly, an increase from $1.77W$ to $2.5W$ causes the high pressure regions located at the upper side regions to move to the lower side regions. Despite a relatively long averaging time, a slight asymmetry in the vertical vortices inside $G_{front}=2.5W$ is evident. This may suggest that it is difficult for the flow to lock in

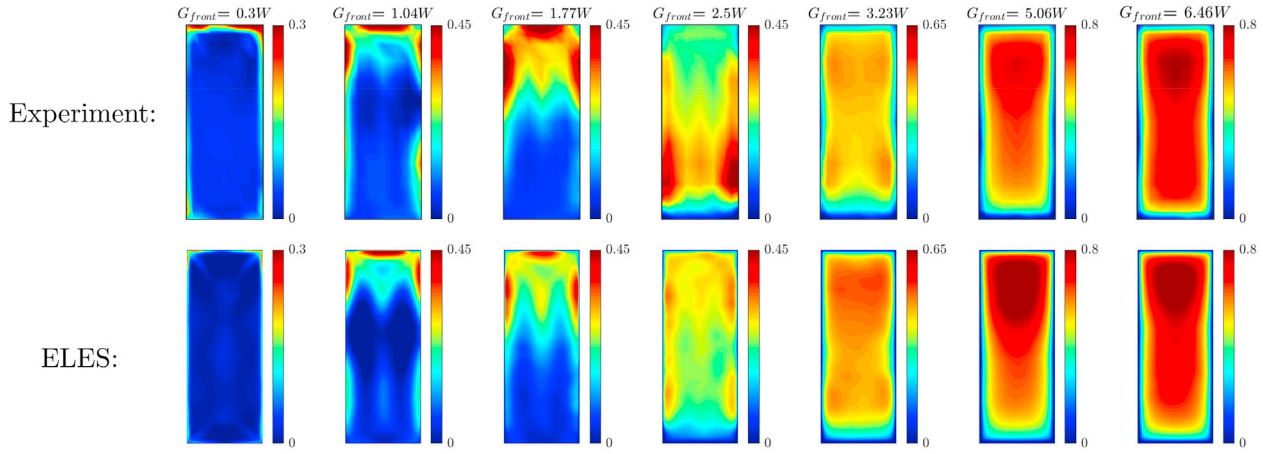

Fig. 6. Wind-tunnel Li et al., (2017) and ELES pressure coefficient (C_p) distributions on the front surface, presented for varying front (G_{front}) gap sizes at a constant $G_{base} = 0.3W$.

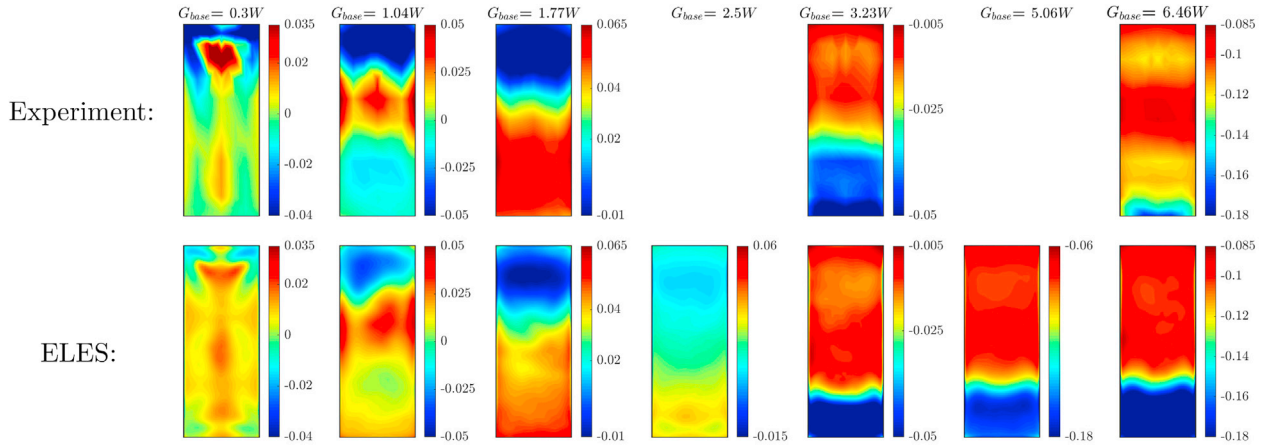

Fig. 7. Wind-tunnel Li et al., (2017) and ELES pressure coefficient (C_p) distributions on the base surface, presented for varying base (G_{base}) gap sizes at a constant $G_{front} = 0.3W$.

a regular periodic shedding state at such a gap size.

At $G_{front} = 3.23W$, the complete wake closure for the upstream wagon occurs, which causes the upstream shear layers to impinge on the entire downstream face. The streamwise length of the two counter-rotating spanwise vortices is evidently shorter than the gap length of $3.23W$ enabling full flow impingement to take place, leading to a significant increase in pressure drag. The pressure contour at $G_{front} = 3.23W$ exhibits an overall uniform pressure, with the sudden drop in pressure magnitude towards all four edges. Such a pressure distribution reflects that of an isolated wagon, only with a lower pressure magnitude. Hence, increasing G_{front} over the front gap range $1.77W$–$3.23W$ changes the mean flow topology, with the impingement of upstream shear layers on the upper region of the front surface transitioning to full flow impingement over the entire front face. This finding is in line with the suggested flow regime change over the gap range $1.77W$–$3.23W$ proposed by Li et al. (2017), although the experimental measurement techniques were not able to verify that this was indeed the case.

At $G_{front} \geq 5.06W$, the predictions show that the flow impingement on the front surface occurs with higher momentum being transferred from the freestream flow, resulting in a higher pressure drag. No significant change in mean flow topology is evident as G_{front} is increased between $5.06W$ and $6.46W$, except for the more complete recovery of the impinging flow towards the uniform background flow. Thus, increasing G_{front} beyond $5.06W$ only causes the front surface pressure distribution to increase slightly.

Fig. 10 shows predictions of time-averaged projected streamlines in the $z = 0$ plane for varying G_{base} at a constant $G_{front} = 0.3W$. Once again, the flow field inside the base gap at $G_{base} = 1.04W$ consists of two counter-rotating vortices, where the flow attachment on the rear of the test wagon occurs in between them causing the higher pressure region. This wake topology is consistent with the presence of three bands of pressure on the base surface at $G_{base} = 1.04W$, where the band of highest pressure is sandwiched between the two low pressure bands, as presented in Fig. 7.

At $G_{base} = 1.77W$, a similar low pressure band to $G_{base} = 1.04W$ is apparent at the top. However, the bottom low pressure has disappeared and the high pressure region has extended downwards close to the ground. This can be explained by an increase in the upper spanwise vortex and the disappearance of the lower spanwise vortex, leaving a large space on the bottom of the base for the impingement of the side shear layers, as displayed in Fig. 10. No significant change in wake topology can be seen as the downstream gap increases from $1.77W$ to $2.5W$, except a further increase in the upper spanwise vortex. The C_p on the entire base surface remains almost close to zero over this range. Note that no experimental data is available for comparison at $G_{base} = 2.5W$ and $5.06W$, as mentioned earlier.

With an increase of $G_{base} = 2.5W$ to $G_{base} = 3.23W$, the wake profile once again undergoes a significant change. Two spanwise vortices are again appeared inside the gap. The wake closure also occurs inside $G_{base} = 3.23W$ similar to the one observed inside $G_{front} = 3.23W$, despite

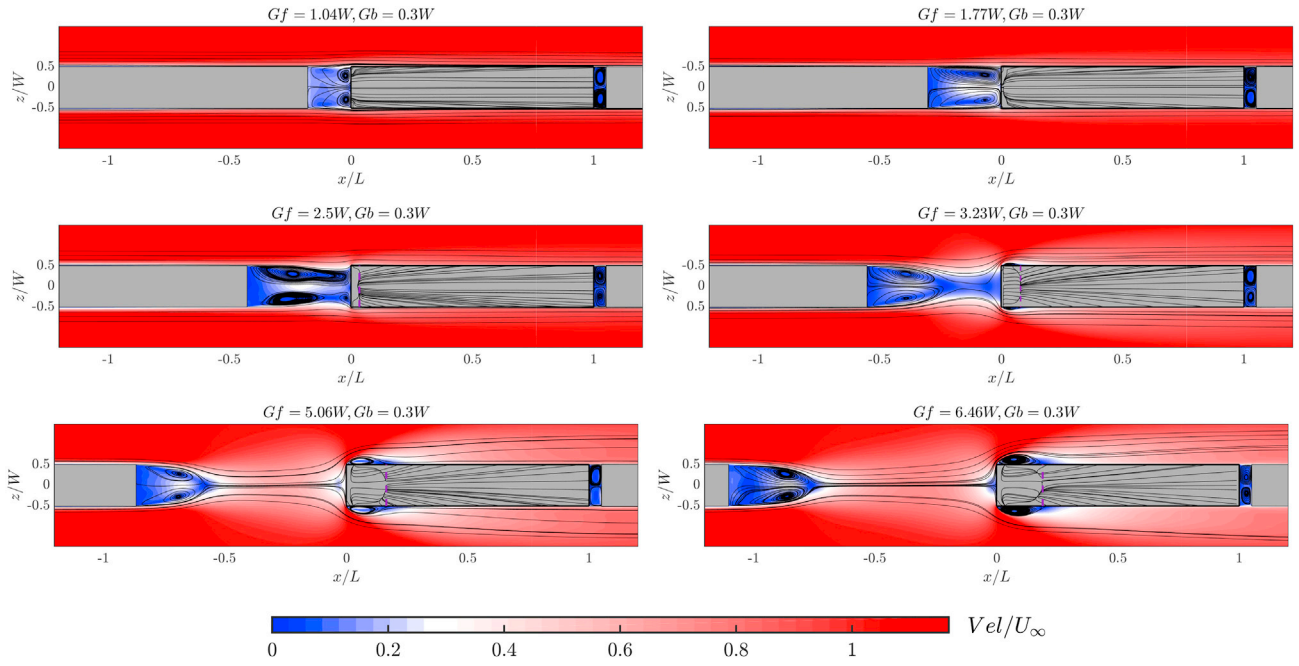

Fig. 8. Top-down view of predicted time-averaged streamlines in the $x - z$ plane at $y = H/2$ for varying front (G_{front}) gap sizes at a constant $G_{base} = 0.3W$. The purple dashed lines show reattachment lines on the top surface of the test wagon. The surface streamlines on the upper surface are also shown. (For interpretation of the references to colour in this figure legend, the reader is referred to the Web version of this article.)

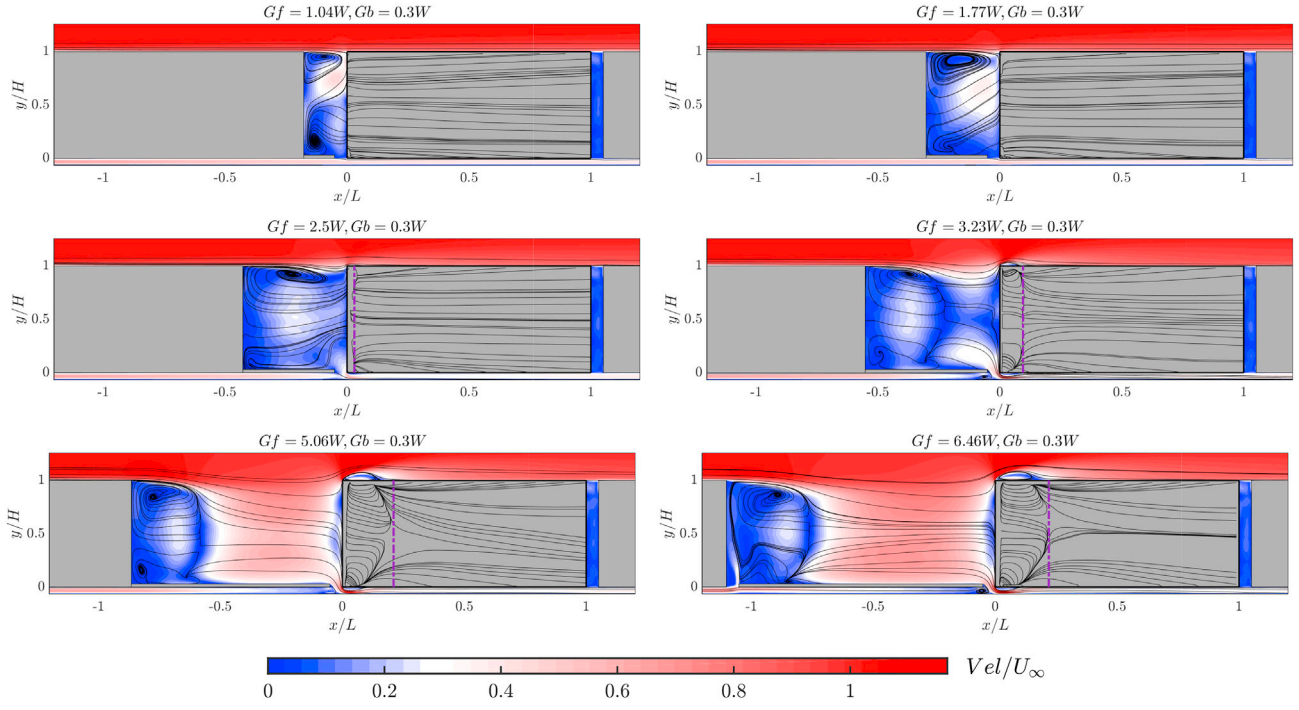

Fig. 9. Side-view of predicted time-averaged streamlines in the x–y plane at $z = 0$ for varying front (G_{front}) gap sizes at a constant $G_{base} = 0.3W$. The purple dashed lines show reattachment lines on the side surface of the test wagon. The surface streamlines on the side surface are also shown. (For interpretation of the references to colour in this figure legend, the reader is referred to the Web version of this article.)

the opposite placement of the empty wagon surface inside the upstream and downstream gap size.

It is apparent that further increases of $G_{base} = 3.23W$ cause no discernible global change to the wake topology. Only the magnitude of base pressure continues to drop as G_{base} is enlarged, due to the increase of base suction. The base pressure for $G_{base} \geq 5.06W$ exhibits a similar pressure distribution to a single wagon in freestream showing two pressure bands, where the low pressure region is on the lower part of the base surface. The wake closure mechanism for gap size of $\geq 3.23W$ is dominated by the inflow from the sides of the model rather than the top since the streamlines bounding the recirculation bubble are almost vertical for the majority of the wagon height. Due to the close proximity of the downstream wagon to the upstream one at gap size of $3.23W$, some of the reversed flow entering the wake originates from the downstream

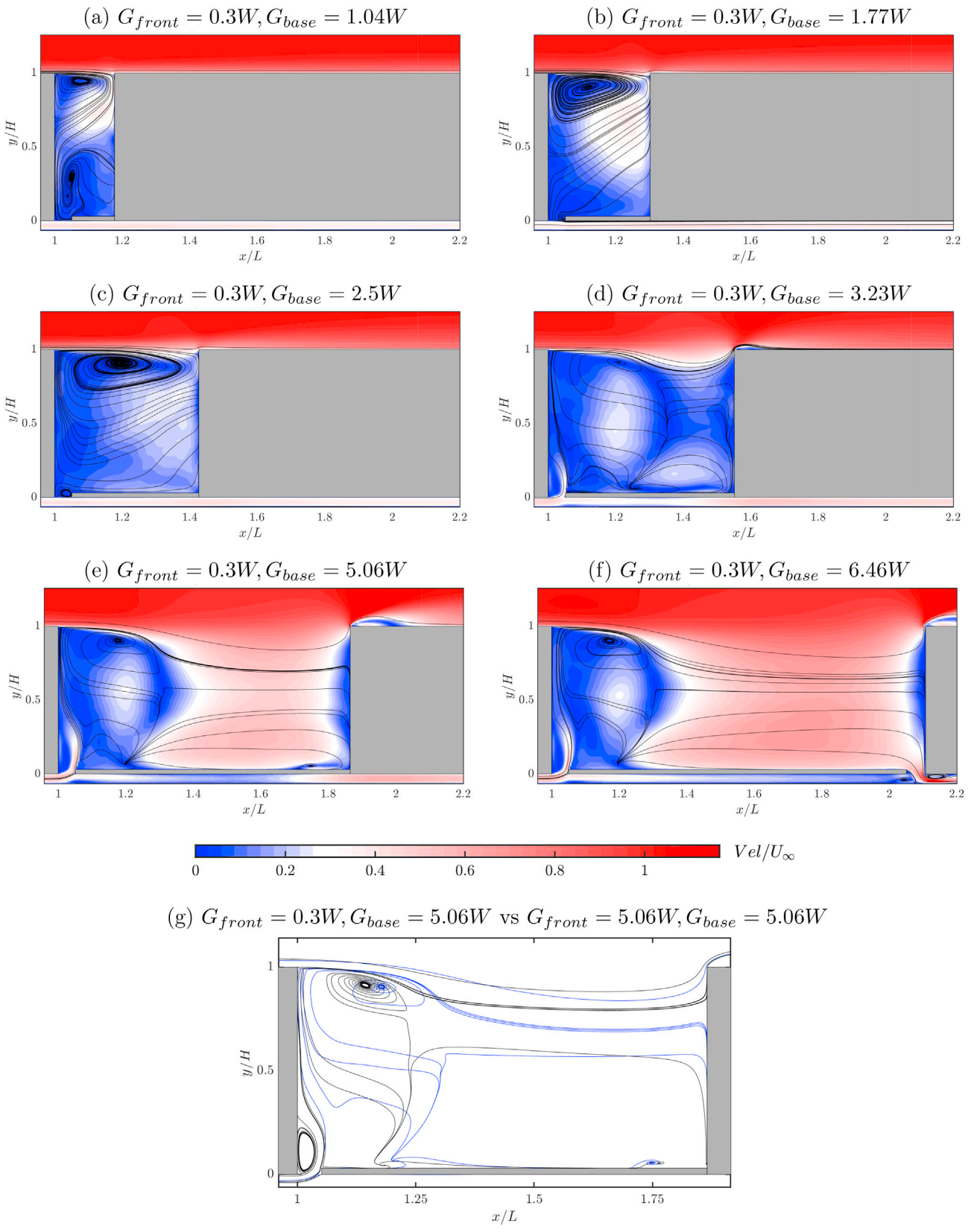

Fig. 10. (a–f) Side-view of predicted time-averaged streamlines on x–y plane at $z = 0$ for varying base (G_{base}) gap sizes at a constant $G_{front} = 0.3W$. (g) Comparison of side-view mean streamlines inside the downstream gap between $G_{front} = 0.3W$ and $G_{base} = 5.06W$ (blue) and $G_{front} = 5.06W$ and $G_{base} = 5.06W$ (black). (For interpretation of the references to colour in this figure legend, the reader is referred to the Web version of this article.)

model. The upper vortex formed behind the wagon subjected to the gap size of $\geq 3.23W$ shows similarity to that observed behind the GTS model at the lowest ground clearance reported in Fig. 25a of McArthur et al., (2016).

Finally, Fig. 10.g shows the comparison between the time-averaged streamlines inside $G_{base} = 5.06W$ for $G_{front} = 0.3W$ and $G_{front} = 5.06W$. It is clear that an increase in the upstream gap size causes the size of the wake inside the downstream gap size to be reduced. This aspect is further discussed in Section 6.2.1.

6.1.2. Reynolds stresses

To better understand the flow dynamics contributing to the resultant mean flow, the Reynolds stress components in the $y = 0.5H$ and $z = 0$ planes, along with bounding streamlines (defining the extent of the recirculation zones) are presented in Figs. 11 and 12, respectively. These are defined as covariances of fluctuating velocity components with the figures showing their local intensities POPE, (2000). Note that only the $\overline{u'v'}$ and $\overline{u'w'}$ shear stress components are shown due to the large number of cases.

Fig. 11 clearly shows the concentration of velocity fluctuations along the separating shear layers and extending downstream from the mean recirculation zones. It can be seen that an increase in G_{front} results into a contraction of the wake at a constant $G_{base} = 5.06W$, while no discernible change in the size of the wake can be seen for $G_{base} \geq 3.23\,W$at a constant $G_{front} = 0.3W$. The shrinkage of the wake causes the base pressure to drop, as the low pressure cores move closer to the behind of the model, leading to a higher drag. The reduction in the length of the time-averaged wake inside G_{base} can be explained by the increase in the shear layer curvature due to the higher turbulence at the trailing edge of the model induced by the large G_{front}.

Fig. 12 shows the intensity of the shear stresses $\overline{u'v'}$ occurring along the upper shear layers reduces with an increase of G_{base}. Evidently, this is related to the presence of the downstream wagon, increasing the velocity fluctuations in the vertical direction immediately downstream of the recirculation zone for smaller G_{base}. In addition, the higher intensity of velocity fluctuations along the upper shear layers is apparent for all cases. This indicates the unsteadiness along the upper shear layers is slightly stronger than that of the lower shear layer, perhaps due to the larger size of the vortex formed on the upper side of the base but also likely to be a result of the more constrained flow towards the unoccupied wagon surface. Once again, the high height-to-width ratio of the wagon as well as the presence of the unoccupied wagon surface inside G_{base} hinders the interaction of the separating upper shear layer with the lower one originating from beneath the wagon.

6.2. Transients

6.2.1. Frequency analysis

Spectral analysis was used to evaluate the dominant flow frequencies at the front and rear surfaces of the test wagon for different gap combinations. These predictions are given in Tables 2 and 3. The experimental frequencies provided were obtained from pressure taps on the front and base surfaces in wind tunnel experiments. It is clear that the predicted shedding frequencies based on width, $St_w \equiv fW/U_\infty$, match those found in the wind-tunnel experiments within ± 0.01. Note, as mentioned earlier, no experimental data is available for $G_{base} = 5.06W$. In line with the wind-tunnel results, no dominant shedding frequency on both front and base surfaces was detected for the gap sizes below $3.23W$. It is apparent that the shedding frequency inside the front gap increases due to an increase in G_{front}; from $St_w = 0.19$ to $St_w = 0.25$, as G_{front} is increased from $3.23W$ to $6.46W$. Similarly, ELES predictions show that an enlargement of G_{base} causes the rate of shedding to increase from $St_w = 0.19$ to $St_w = 0.23$.

As is shown by Rowe et al. (2001), the vortex shedding frequency of a square-back bluff body is influenced by the boundary-layer thickness upstream of its trailing edge. Hence, the increase in the shedding frequency as the gap size is increased may be associated with local thinning of the side boundary layer at the trailing edge of the wagon located upstream of the gap, as the fluid is accelerated and deflected to enter the gap rather than to flow over the top of it. This is also consistent with the formation of a slightly larger wake for $G_{base} = 3.23W$ than $G_{base} \geq 5.06W$. Of course, the presence of the front surface of the downstream wagon has a strong influence on the gap flow dynamics.

Having tested a combination of 49 upstream and downstream gap size combinations, Li et al. (2017) managed to quantify the effect of the variation of the upstream and downstream gap size on shedding frequency measured within the opposite gap. They reported that an increase in the upstream gap size reduces the shedding frequency within the downstream gap, while varying the downstream gap has little influence on the shedding frequency inside the upstream gap as the downstream flow condition does not propagate to the upstream flow. Table 3 shows

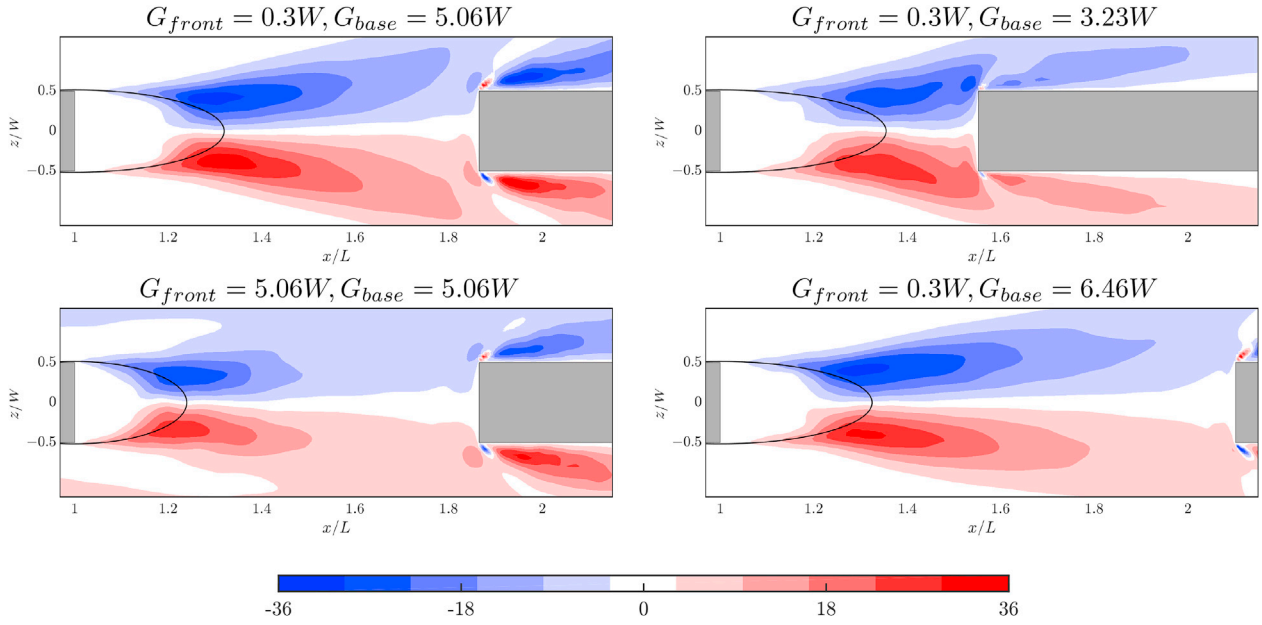

Fig. 11. Predicted $\overline{u'w'}$ Reynolds stress distribution for different gap combinations. The solid lines indicate the extent of the recirculation zone.

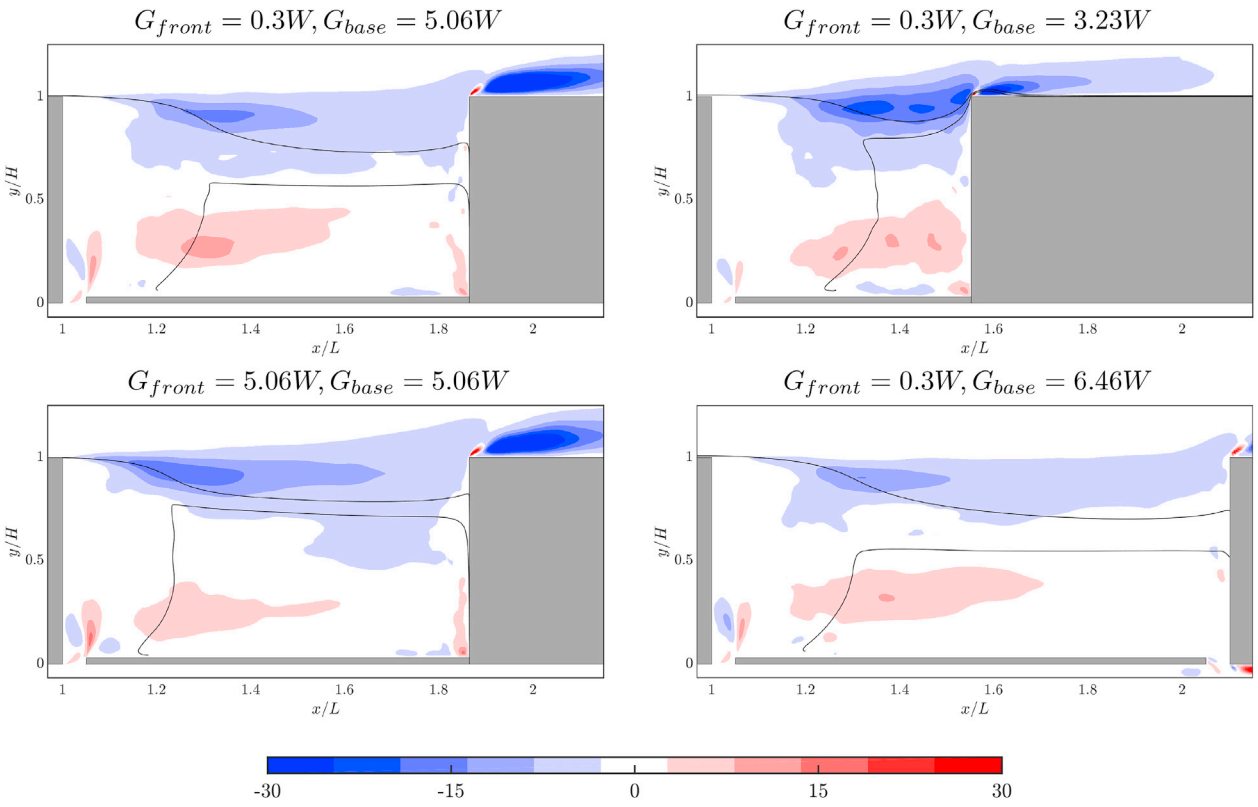

Fig. 12. Predicted $\overline{u'v'}$ Reynolds stress distribution. See Fig. 11 for further details.

Table 2
Wind-tunnel and ELES non-dimensional shedding frequency St_w detected at the front surface.

			G_{front}		
			3.23W	5.06	6.46
G_{base}	ELES	0.3W	0.195	0.25	0.25
		5.06W	0.2	0.24	–
G_{base}	Exp	0.3W	0.19	0.25	0.25

Table 3
Wind-tunnel and ELES non-dimensional shedding frequency St_w detected at the base surface.

			G_{base}		
			3.23W	5.06	6.46
G_{front}	ELES	0.3W	0.19	0.22	0.23
		3.23W	–	0.2	–
		5.06W	–	0.18	–
G_{front}	Exp	0.3W	0.19	–	0.22

the reduction in shedding frequency inside $G_{base} = 5.06W$ from $St_w = 0.22$ to $St_w = 0.18$, as the upstream gap increases from $0.3W$ to $5.06W$. The drop in shedding frequency is once again related to the development of the side boundary layer thickness. For bodies with a square back, Hoerner (1965) and recently Mariotti and Buresti (2013) showed that an increase in a separating boundary layer thickness induces less momentum from the freestream flow being entrained into the wake. Fig. 13 displays the boundary layer thickness along the side of the test wagon for various G_{front} at a constant $G_{base} = 5.06W$. These results clearly indicate that the larger frontal separation associated with the larger upstream gap creates a wider effective width of a wagon, causing the shedding frequency to drop inside $G_{base} = 5.06W$.

7. Containers arrangements optimisation

As this study is motivated by overall train aerodynamic drag, it is useful to understand which loading configuration may provide the greater opportunity for drag reduction. Li et al. (Fig. 28 in Li et al., (2017)) has provided the drag estimation on the double-stacked configuration within a train under various loading patterns. They showed that it is more efficient to avoid as many number of gaps as possible. However, in a situation where gaps are unavoidable, having one large gap size is more favourable for drag saving than multiple moderately sized gaps of the same total length. As discussed in the introduction however, freight trains consist of both single-stacked and double-stacked containers. This means that it is still unknown to engineers how drag changes with the introduction of single-stacked containers adjacent to double-stacked containers. To answer this question, three more ELES simulations were performed, simulating the most common loading patterns in which a single-stacked container(s) is (are) placed at the smallest inter-wagon gap size to a double-stacked container(s). Fig. 14 shows the drag of these loading configurations, normalised against the drag of configuration 1.

It is clear, when an empty wagon can be avoided, it is more favourable to fill the gap with a double-stacked container. However, this is not always possible. These results show one double stacked gap (Configuration 1) is to be preferred over two single stacked gaps either side of a double stacked (Configuration 3). But, adjacent single stacked wagons (Configuration 2) offer a drag saving benefit of 35% compared to Configuration 1. While large gaps are to be avoided, by loading single-stacked containers on an empty wagon in Configuration 3, the space on top of the single-stacked containers enables the flow to fully impinge on the top part of the double-stacked containers front face, causing the drag penalty to be increased. Configuration 4 has been included, noting that it has less containers (or more container gaps) than the other configurations, as it shows little change in the drag for three adjacent slots compared to two adjacent slots (Configuration 2).

Whilst the drag savings associated with Configuration 2 are to be

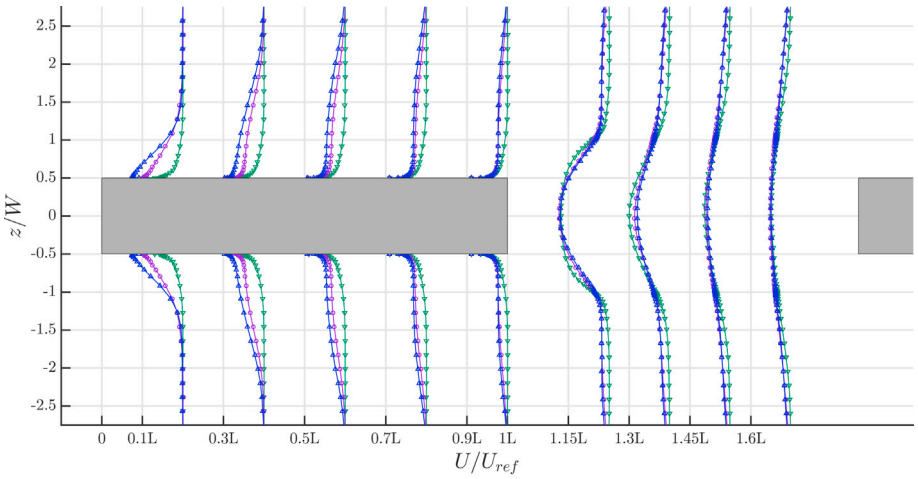

Fig. 13. ELES predictions of time-averaged streamline velocity profile at $x - z$ plane at $Y = 0.5H$ at the side of the test wagon and inside the base gap for varying G_{front} at a constant $G_{base} = 5.06W$.

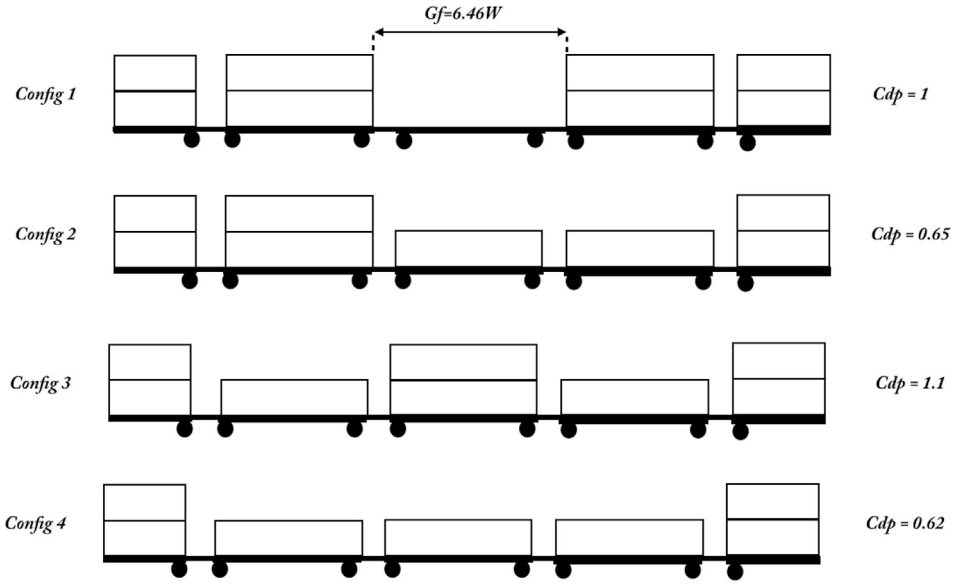

Fig. 14. Drag for various loading patterns.

expected, it is enlightening that one double stacked gap (Configuration 1) results in 10% lower drag than the distributed single gaps in Configuration 3. Therefore, it is not only the length of the gap, but also the length to width ratio of the gap which affects drag.

Following on from this study, there is still a need to improve our understanding regarding the influence of container's arrangement. Specifically, how the drag of a single-stacked and a double-stacked container changes when they are placed close to each other at different gap sizes. Additionally, it is necessary to broaden our knowledge regarding the nature of boundary layer along a freight train, particularly the influence of boundary layer thickness on the aerodynamic drag of a wagon. Furthermore, the freight train aerodynamics under cross-winds needs to be investigated as it is not yet well understood.

8. Conclusions

The flow around a section of a model freight train loaded with different configurations of double-stacked containers has been simulated using the Embedded Large Eddy Simulation (ELES) approach. While an increase of either the front or base gap sizes (G_{front}, G_{base}) surrounding a double-stacked test wagon increased its drag, changing the front gap size had a much stronger effect, in line with published wind-tunnel tests. The time-averaged near-wake consists of pairs of symmetric vortices (top-down view) and vertically asymmetric vortices (side-view). For $G_{front} \leq 1.77W$, the recirculating flow within the front gap shields it from entrainment of the upstream wagon shear layers, allowing them to advect across to the downstream wagon. However, wake closure within the gap begins to occur for $G_{front} = 3.23W$, causing shear-layer flow impingement on the front surface of the test wagon, resulting in high rate of drag growth. The mean recirculation zone of the test wagon was contracted on increasing G_{front} for constant G_{base}, caused by higher turbulence transport out of the near wake, increasing the flow entrainment, and subsequently the curvature of the shear layers.

Having identified the flow mechanism responsible for the high rate of drag increase over this critical gap range, recommendations are provided here to rolling-stock engineers on how to prevent the wake closure for

gap sizes of $\geq 3.23W$. In a situation where the position of one of the (double-stacked) containers subjected to this critical gap size cannot be changed by replacing it with a (double-stacked) container of increased length to reduce the gap spacing, it may be more beneficial to change the wagon type/railroad car to reduce the gap spacing between the two double-stacked containers. As the smallest inter-wagon gap size between different types of wagon vary, engineers may be able to choose a different wagon type to address the problem. However, given the cost and life span, the option of changing rolling stock may not be a practical solution. In a situation where larger minimum gap sizes are unavoidable, adding extenders to the top/side surfaces of the upstream (double-stacked) containers, partially covering the gap, should help the separating boundary layer from entering the gap and impinging of the next container, leading to drag reduction benefits. Additionally, it was shown that there is an opportunity to save the drag increment by 35%, where an empty wagon adjacent to a double-stacked container could be avoided, through placing one of the containers of a double-stacked container on the empty wagon.

The wake shedding frequency was detected for a gap size of $\gtrsim 3.23W$ and it increased as the gap size was enlarged. This increase in shedding frequency for a large gap size was consistent with the decrease in the side boundary thickness at the trailing edge of the wagon located upstream of the gap due to the base suction, thus decreasing the effective width of a wagon. In addition, it was found that the frontal separation generates the flow structures governing the dominant wake frequency. Larger G_{front} induces a thicker side boundary layer at the trailing edge of the wagon due to the higher frontal separation, creating a wider effective width of the wagon, thereby reducing the shedding frequency. For a double-stacked wagon with a relatively higher height-to-width ($H/W = 2.56$) ratio, the separating side shear layers fed the vortex shedding and these governed the dominant frequency in the wake.

Acknowledgement

The research described in this paper was supported by Pacific National Rail and an Australian Research Council Linkage Project Grant LP13100953. SM would also like to acknowledge partial PhD scholarship funding through this grant.

References

Ahmed, S., 1983. Influence of base slant on the wake structure and drag of road vehicles. ASME J. Fluids Eng 105 (4), 429–434.
Bell, J.R., Burton, D., Thompson, M.C., Herbst, A.H., Sheridan, J., 2016. Dynamics of trailing vortices in the wake of a generic high-speed train. J. Fluid Struct. 65, 238–256.
Fago, B., Lindner, H., Mahrenholtz, O., 1991. The effect of ground simulation on the flow around vehicles in wind tunnel testing. J. Wind Eng. Ind. Aerod. 38 (1), 47–57.
Gielow, M.A., Furlong, C.F., 1988. Results of Wind Tunnel and Full-Scale Tests Conducted from 1983 to 1987 in Support of the Association of American Railroads' Train Energy Program. Technical report.
Golovanevskiy, V.A., Chmovzh, Vitaly V., Girka, Yuriy V., 2012. On the optimal model configuration for aerodynamic modeling of open cargo railway train. J. Wind Eng. Ind. Aerod. 107, 131–139.
Hoerner, S.F., 1965. Fluid-Dynamic Drag: Practical Information on Aerodynamic Drag and Hydrodynamic Resistance. Hoerner Fluid Dynamics.
J Baker, C., Quinn, A., Sima, M., Hoefener, L., Licciardello, R., 2014. Full-scale measurement and analysis of train slipstreams and wakes. part 1: ensemble averages. Proc. Inst. Mech. Eng. - Part F J. Rail Rapid Transit 228 (5), 451–467.
Krajnović, S., Davidson, L., 2005. Influence of floor motions in wind tunnels on the aerodynamics of road vehicles. J. Wind Eng. Ind. Aerod. 93 (9), 677–696.
Li, C., Burton, D., Kost, M., Sheridan, J., Thompson, M.C., 2017. Flow topology of a container train wagon subjected to varying local loading configurations. J. Wind Eng. Ind. Aerod. 169, 12–29.
Maleki, S., Burton, D., Thompson, M.C., 2017. Assessment of various turbulence models (eles, sas, urans and rans) for predicting the aerodynamics of freight train container wagons. J. Wind Eng. Ind. Aerod. 170, 68–80.
Mariotti, A., Buresti, G., 2013. Experimental investigation on the influence of boundary layer thickness on the base pressure and near-wake flow features of an axisymmetric blunt-based body. Exp. Fluid 54 (11), 1612.
Mathey, F., Cokljat, D., Bertoglio, J.P., Sergent, E., 2006. Specification of les inlet boundary condition using vortex method. Prog. Comput. Fluid Dynam. Int. J. 6, 58–67.
McArthur, D.J., Burton, D., Thompson, M.C., Sheridan, J., 2016. On the near wake of a simplified heavy vehicle. J. Fluid Struct. 66, 293–314.
F. Menter. Best Practice: Scale-Resolving Simulations in Ansys Cfd.
Östh, J., Krajnović, S., 2012. The flow around a simplified tractor-trailer model studied by large eddy simulation. J. Wind Eng. Ind. Aerod. 102, 36–47.
Paul, J.C., Johnson, R.W., Yates, R.G., 2009. Application of cfd to rail car and locomotive aerodynamics. In: The Aerodynamics of Heavy Vehicles II: Trucks, Buses, and Trains. Springer, pp. 259–297.
POPE, S.B., 2000. Turbulent Flows.
Rowe, A., Fry, A.L.A., Motallebi, F., 2001. Influence of boundary-layer thickness on base pressure and vortex shedding frequency. AIAA J. 39 (4), 754–756.
Strachan, R.K., Knowles, K., Lawson, N.J., 2007. The vortex structure behind an ahmed reference model in the presence of a moving ground plane. Exp. Fluid 42 (5), 659–669.
Watkins, S., Saunders, J.W., Kumar, H., 1992. Aerodynamic drag reduction of goods trains. J. Wind Eng. Ind. Aerod. 40 (2), 147–178.